Mean kinetic energy transport and event classification in a model wind turbine array versus an array of porous disks: Energy budget and octant analysis

Elizabeth H. Camp and Raúl Bayoán Cal

Phys. Rev. Fluids **1**, 044404 — Published 1 August 2016

DOI: 10.1103/PhysRevFluids.1.044404

Mean kinetic energy transport and event classification in a model wind turbine array versus an array of porous disks: energy budget and octant analysis

Elizabeth H. Camp* and Raúl Bayoán Cal†

Portland State University, Department of Mechanical and Materials Engineering

(Dated: June 29, 2016)

Abstract

An array of model rotating wind turbines is compared experimentally to an array of static porous disks in order to quantify the similarities and differences in the mean kinetic energy transport within the wakes produced in these two cases. Stereo particle image velocimetry measurements are done in a wind tunnel bracketing the center turbine in the fourth row of a 4×3 array of model turbines. **Equivalent sets of rotors and porous disks are created by matching their respective induction factors. The primary difference in the mean velocity components was found in the spanwise mean velocity component, which is much as 190% different between the rotor and disk case.** Horizontal averages of mean kinetic energy transport terms in the region where rotation is most important show percent differences in the range 3-41% which decrease to 1-6% at streamwise coordinates where rotation is less important. Octant analysis is performed on the most significant term related to vertical mean kinetic energy flux, $\overline{u'v'}U$. The average percent difference between corresponding octants is as much as 68% different in the near wake and as much as 17% different in the far wake. Furthermore, octant analysis elucidates the three dimensional nature of sweeps and ejections in the near wake of the rotor case. Together, these results imply that a stationary porous disk adequately represents the mean kinetic energy transport of a rotor in the far wake where rotation is less important while significant discrepancies exist at streamwise locations where rotation is a key phenomenon. This comparison has implications on the use of an actuator disk to model the wind turbine rotor in computational simulations **specifically for studies where Reynolds stresses, turbulence intensity, or interaction with the atmosphere are of interest**.

* betsy.h.camp@gmail.com

† rcal@pdx.edu

I. INTRODUCTION

The power production capacity from wind energy continues to increase as new wind turbines and wind turbine arrays are installed worldwide [1]. Wind turbine wakes can persist more than fifteen rotor diameters (D) downstream of wind turbines [2], while the spacing in many operational wind farms is much less than this distance and hence many turbines are influenced by the wake of neighboring turbines. Thus, in a wind farm, the wakes of upstream turbines affect the power production [3],[4], dynamic loading [5], and fatigue characteristics [6] of turbines downstream. Wind turbine wakes in wind turbine arrays also interact with the atmospheric boundary layer (ABL) which, in turn, affects the surface heat flux [7] from the earth in the vicinity of the turbines and, in large farms, may influence local micrometerology [8]. Since wind turbine wakes are key in all of these phenomena, from power production to atmospheric influence, it is critical to understand and predict these wakes.

Both experimental measurements and computational fluid dynamics (CFD) work has contributed to the understanding of wind turbine wakes as well as the ability to predict such flows [9]. Among computational codes based on the Navier-Stokes equations, turbulence models based on Reynolds Averaged Navier Stokes (RANS) as well as Large Eddy Simulations (LES) are the current state-of-the-art for flows involving wind turbines and wind farms [10]. In addition to a turbulence model, a model for the wind turbine rotor is needed in CFD simulations. Two such turbine models are the actuator disk (AD) model and the actuator line (AL) model [11]. In computational work, the calculated data is influenced by both the turbulence model and rotor model used to generate it.

Studies have been performed to compare different turbine models used in computational simulations to determine their impact on the resulting computed data. Wu and Porté-Agel [12] compared LES simulations of two different AD models to a physical wind turbine model in a wind tunnel. Both AD models resulted in flow fields that differed dramatically from one another and from the measured wind tunnel turbine model in the near wake. The mean velocity components of all three cases became quite similar by five rotor diameters downstream while turbulence intensity and Reynolds shear stress still showed discrepancies until $10D$ and $20D$ downstream, respectively. Martínez-Tossas *et al.* [13] compared LES simulations of an AD model and AL model with wind tunnel measurements of a model turbine having a rotor with the same airfoil profile. While the mean velocity profiles of the AD and AL models were nearly the same in the near wake, they differed from the wake of the wind tunnel model directly downstream of the turbine. Power production estimates of the two turbine computational models differed by less than 1%.

In the wind energy context, it is difficult to create equivalent computational simulations and wind tunnel simulations for comparison [14]. Some of these challenges arise during the calculation of the turbine model parameters to be used in the CFD simulation ~~using the blade element approach~~ due to uncertainty in the physical blade profile [15], [16]. Such issues have motivated the use of physical experiments to compare the wakes from actuator disk modeled turbines with those from turbines modeled using rotors. Wind tunnel measurements by Aubrun *et al.* [17] performed utilizing hot-wire anemometry compared the physical equivalent of an actuator disk, a stationary porous disk, with a matched turbine model having a three-bladed rotor under two inflow conditions. The mean streamwise velocity as well as the skewness and kurtosis of the streamwise velocity between the porous disk and rotor display the most significant disparities in the near wake. However, by three diameters downstream, they became nearly the same. Lignarolo *et al.* [18] used stereo particle image velocimetry (PIV) to measure the wake between $0.1D$ and $2.2D$ downstream of a porous disk and matched model wind turbine rotor in a wind tunnel with uniform inflow. The greatest differences in the flow characteristics were found at small downstream distances. However, by $2.2D$ downstream, the axial velocity and all three components of the turbulence intensity were nearly identical. Of the quantities compared, the greatest disparities between rotor and disk cases were in the mean kinetic energy transport at the turbine model edge.

Single wind turbines and turbines at the periphery of wind farms function differently than those positioned within a wind turbine array [3], [19]. This has made it necessary to conduct studies on model wind turbine arrays (e.g., [20], [21]) to augment knowledge gained from work done on single turbines. Similarly, studies are needed to compare the flow fields from an array of porous disks with an array of model turbines having rotors.

The similarities and differences in the wakes of porous disk modeled turbines and three-bladed model turbines deep within a turbine array are examined via a wind tunnel experiment. The present analysis of the mean kinetic energy budget in both the near and far wake allows a detailed comparison of terms relevant to power production in wind farms as well as interaction with the fluid above the array. The interaction of turbine wake with the fluid above the turbine array is investigated since energy exchange between the fluid above and within the array accounts for a significant influx of the kinetic energy allowing wake remediation in large wind farms [20], [21], [22]. In addition, octant analysis is used to conditionally average the term most relevant to vertical mean kinetic energy flux in order to link the direction of the velocity fluctuations to the vertical entrainment of mean kinetic energy. From octant analysis, inferences can be made so as to contrast the mechanism by which mean kinetic energy is brought into the array from aloft in the two model farms.

II. THEORY

The equation for the kinetic energy of the mean flow can be found by taking the scalar product of the RANS equation with the mean velocity and contracting free indicies to obtain

$$U_j \frac{\partial K}{\partial x_j} = \frac{\partial}{\partial x_j} \left\{ -\frac{1}{\rho} P U_i \delta_{ij} - \overline{u_i' u_j'} U_i + 2\nu S_{ij} U_i \right\} + \overline{u_i' u_j'} \frac{\partial U_i}{\partial x_j} - 2\nu S_{ij} S_{ij}, \tag{1}$$

with $U_1 = U$, $U_2 = V$, $U_3 = W$ being the streamwise, wall-normal, and spanwise components of the mean velocity, respectively. The corresponding fluctuating components are denoted with lower case and primes. For example, $u_1' = u'$ indicates the fluctuating component of the streamwise velocity. Time averaging is denoted using an overline ($\overline{[...]}$) on the time-averaged quantities. The advection of mean kinetic energy is expressed as $\boldsymbol{U_j \partial K/\partial x_j}$ ~~K~~ in Eq. (1) and **where $\boldsymbol{K}$** is defined using the relation $K = (1/2)U_i U_i$, where $i = 1$, 2, and 3. The three terms shown in curly braces ($\{\}$) on the right hand side of Eq. (1) represent the transport of mean kinetic energy by the pressure gradient, transport of mean kinetic energy by the turbulence itself, and transport due to viscosity, respectively. The production of turbulent kinetic energy (TKE) is represented by $\overline{u_i' u_j'} \partial U_i/\partial x_j$ which acts as a route for energy to be exchanged between the mean **flow** and the fluctuations. The production term often acts to decrease the kinetic energy of the mean flow while adding energy to the fluctuations. The dissipation of mean kinetic energy directly to internal energy is expressed as $-2\nu S_{ij} S_{ij}$, where the mean strain rate is defined by $S_{ij} = 1/2 \left(\partial U_i/\partial x_j + \partial U_j/\partial x_i \right)$. Since $S_{ij} S_{ij}$ is always a positive quantity, the dissipation term always acts to remove kinetic energy from the mean flow. Terms expressing the thrust of the turbines have not been included in Eq. (1) since the model turbines are just outside the measurement region.

In order to further investigate the vertical transport of mean kinetic energy, conditional

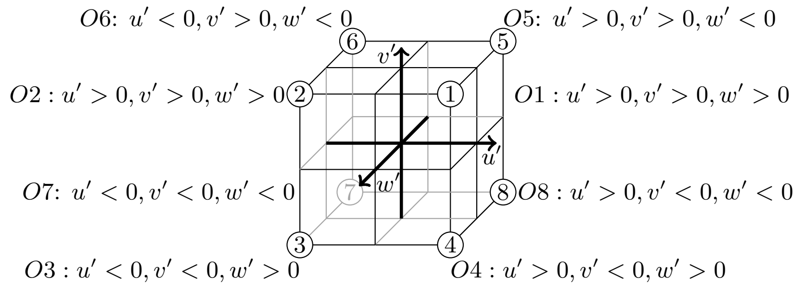

Figure 1. Relationship between the octant number and the sign of the fluctuations in the x-, y-, and z-directions given by u', v', and w', respectively. **Octant labels are given as O1-O8.**

averaging is employed. Quadrant analysis is a method of conditional averaging based on categorizing the sign of the instantaneous fluctuations u' and v' [23]. Octant analysis is an extension of this technique based on categorizing the sign of three instantaneous fluctuations namely, u', v', and w'. Figure 1 shows the relationship between the octant number and the signs of u', v', and w'. Octants 2 and 6 both represent sweeps since $u' > 0$ and $v' < 0$ although in $O2$, $w' > 0$ whereas in $O6$ $w' < 0$. Similarly, $O4$ $(u' > 0, v' < 0, w' > 0)$ and $O8$ $(u' > 0, v' < 0, w' < 0)$ both denote ejections. Outward interactions are represented by $O1$ $(u' > 0, v' > 0, w' > 0)$ and $O5$ $(u' > 0, v' > 0, w' > 0)$. Inward interactions are given by $O3$ $(u' < 0, v' < 0, w' > 0)$ and $O7$ $(u' < 0, v' < 0, w' < 0)$. Octant analysis has been used to analyze three dimensional boundary layers such as that near a wing-body junction [24] as well as a case near a prolate spheroid [25].

Conditionally averaged quantities are denoted using the symbol $\overline{\ddot{(...)}}$. The conditional average of the kinetic energy flux term is computed via octant analysis by performing

$$\overline{\ddot{u'v'U}}_k(x,y) = \frac{U(x,y)}{N} \sum_{n=1}^{N} u'_n(x,y) v'_n(x,y) I_k[u'_n(x,y); v'_n(x,y); w'_n(x,y)], \tag{2}$$

where k is the octant number (1-8), n is the ~~signal for~~ **index of** a given sample, N is the total number of samples, x is the streamwise coordinate and y is the wall normal coordinate of the measurement location. The step function I_k is defined as

$$I_k[u'_n(x,y); v'_n(x,y); w'_n(x,y)] = \begin{cases} 1 & \text{if } (u'_n, v'_n, w'_n) \text{ is in octant } k, \\ 0 & \text{if otherwise.} \end{cases} \tag{3}$$

The binning of the instantaneous values of the fluctuations illustrates the instantaneous direction of the fluctuations relative to the mean flow. As a result, the conditional average of the vertical transport of mean kinetic energy, $\overline{u'v'U}$, in Eq. (2) shows the directionality of the fluctuations when mean kinetic energy is transported. Hamilton *et al.* [26] as well as Viestenz *et al.* [27] performed quadrant analysis on hot-wire anemometry measurements done in a wind tunnel in the wake of 3×3 model wind farm. Both studies found that ejections and sweeps were primarily responsible for the vertical transport of mean kinetic energy. Lignarolo *et al.* [28] corroborated this conclusion by performing quadrant analysis on PIV measurements done on a single turbine in uniform flow. In the present study, it is of interest to investigate the role of the spanwise fluctuating velocity component, w', since a rotating wind turbine blade is expected to impart different characteristics to the spanwise velocity component due to the blade rotation than a stationary disk. ~~As a result~~ **To capture the contribution of the spanwise velocity component**, octant analysis is used rather than quadrant analysis.

III. EXPERIMENTAL DESIGN

Experiments are conducted at the facility at Portland State University. This closed-loop wind tunnel has a 9:1 contraction ratio. The test section has a 5 m length with a cross-section of 0.8 m H × 1.2 m W. Figure 2 shows that a passive grid, strakes, and chains are placed upstream of the model wind farm in order to produce an inflow to the farm with characteristics that emulate the atmospheric boundary layer. The acrylic strakes used are identical in geometry to those employed by Cal *et al.* [21].

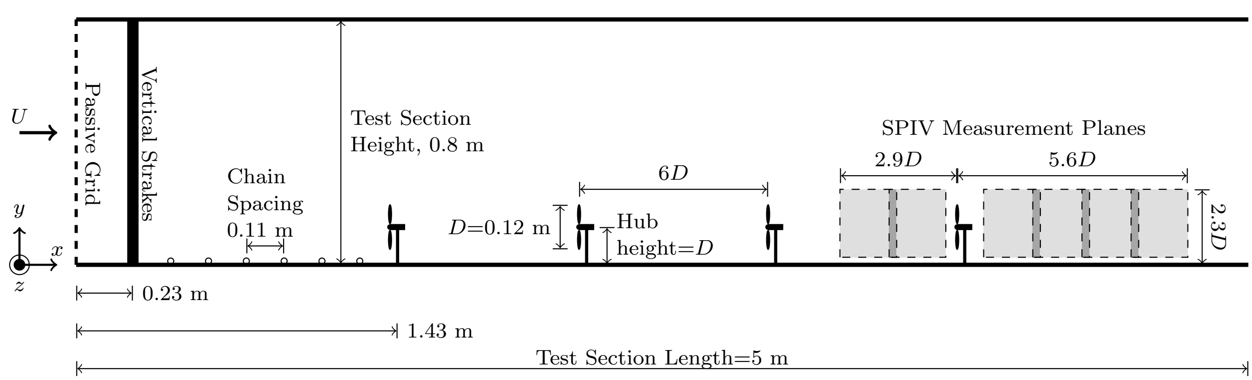

Figure 2. Side view of tunnel test section with experimental apparatus (*for reference only: drawing not to scale*)

The model wind turbine array is composed of four rows of turbines in the streamwise direction ~~with three turbines in each row~~ as shown in Figure 2. **Each row is composed of three turbines with** ~~The~~ **a** cross-stream spacing of ~~the turbines in each row is~~ $3D$ **from hub to hub**. Three-bladed wind turbine models with the dimensions shown in Figure 3(b) are used in this study and are compared to an array of matched porous disks shown in Figure 3(c). Turbine blades are fabricated from 26 gage (0.475 mm) galvanized steel sheet metal which is pressed via a die to give a twist of 15° at the blade tip and 22° at the blade root. Model nacelles are composed of an electric motor (Faulhaber GMBH model 1331T012SR) acting as a generator and loaded such that wind turbines are operating at their peak **power coefficient** (C_p) as described by Hamilton *et al.* [29].

A matched set of twelve porous disks is built to compare with the rotors. Disks are laser cut from 3.2 mm thick plywood. A rapid prototyped adapter is used to mount the disks to the nacelle in order to ensure that downstream surface of the disk is at the same streamwise location as the rotor hub. ~~The design concept of the disk is chosen to conform to the geometric properties of the rotor in that~~ The disk was designed to be circumferentially symmetric ~~and having~~ **with** a ~~varying~~ porosity **that varies** with radial coordinate **in order to mimic the design of the rotor**.

The induction factor is used to match the disks to the rotor. An iterative procedure is applied to arrive at the particular disk design shown in Figure 3(c). The induction factor

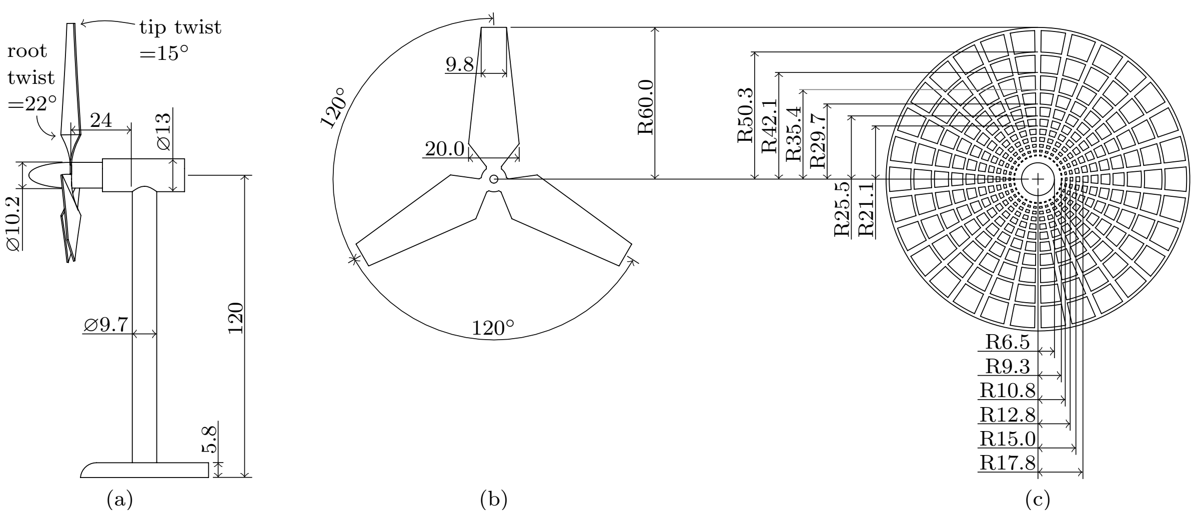

Figure 3. Scale drawings of the geometry of the (a) turbine model with pressed rotor, (b) rotor flat pattern, and (c) porous disk. All dimensions are in millimeters unless otherwise noted. The mounting adapter for the hub of the ~~rotor and~~ disk ~~are~~ **is not shown.**

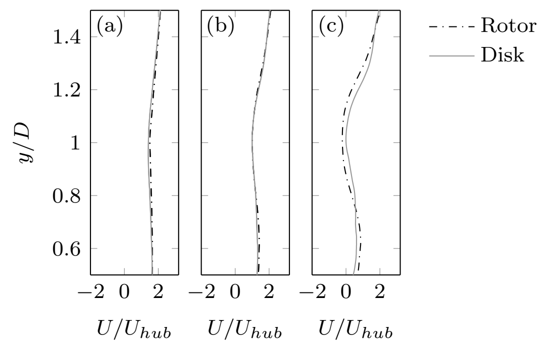

Figure 4. **Profiles of the rotor and disk found during characterization at the position of the first row. The streamwise location of the rotor or disk is** $x/D = 0$**. (a) measured profiles at** $x/D = -0.19$**, (b) computed profiles at** $x/D = 0$**, (c) measured profiles at** $x/D = 0.47$**).**

is calculated from particle image velocimetry measurements of the flow field bracketing the center turbine in the first row. Velocity profiles were taken 23 mm upstream **($\boldsymbol{x/D = -0.19}$)** and 56 mm downstream **($\boldsymbol{x/D = 0.47}$)** of the rotor blade and disk, respectively. Linear interpolation between the upstream and downstream profiles was done to estimate the velocity profile at the disk and rotor, respectively. **Velocity profiles pertinent to the disk characterization phase of the experiment are provided in Figure 4.** The induction factor, a, was then computed from this velocity profile following the method outlined in Cal *et al.* [21]. **The method used by Cal *et al.* to compute** a **from the flowfield relies upon the streamtube concept. This concept is expected to be most accurate when applied in the first row of turbines in the current setup thus making the first turbine row the most appropriate location for disk characterization.** As in Burton *et al.* [30], the corresponding thrust coefficient, C_t, is computed from the induction factor via

$$C_t = 4a(1-a). \tag{4}$$

A summary of the disk and rotor characteristics are provided in Table I. Note that a and C_t are rounded to three significant digits and the percent difference between the induction factors of the disk and rotor is less than 1%. Furthermore, since disk and rotor matching is done in the first row of turbines, Eq. (4) has been applied in the absence of upstream turbine wakes.

Table I. Comparison of disk and rotor characteristics

Characteristic	Disk	Rotor
Diameter (mm)	120	120
a	0.202	0.200
C_t	0.644	0.640

Measurements are carried out using via stereo PIV (SPIV) upstream and downstream of the center turbine in the fourth row. Figure 2 shows the six SPIV planes surrounding the turbine of interest. Each individual plane is approximately 165 mm $W \times 240$ mm H. Measurement planes overlap by approximately $0.1D$. In regions where successive measurement planes overlap, the data **from** the two planes is averaged.

The SPIV system is composed of two LaVision 4 megapixel Pro LX cameras fitted with Schiempflug adapters, a Litron Nano L 200-15 double pulsed Nd:YAG laser, and the software DaVis 8.1.5 by LaVision. The flow is seeded with Diethyl-Hexyl Sebacate that was aerosolized through a seeding generator which uses a Laskin nozzle (LaVision model #1108926). Seeding densities throughout the field of view (FOV) of each camera are consistently held above 0.02 particles per pixel. The laser sheet thickness is 1-1.7 mm throughout the FOV of each camera. Cameras are placed in forward scatter with each camera viewing opposite sides of the laser sheet. The angle between each camera body and the laser sheet is 45 degrees and thus the included angle between the two cameras is 90 degrees. Calibration is done using a two-level calibration plate with markers placed at known locations. Self-calibration is performed on particles in the laser sheet using the method of Weineke [31] as implemented in DaVis version 8.1.5. For each measurement plane, the disk and rotor measurements are carried out in series using the same camera and laser setup and the same camera calibration. Data is collected at a frequency of approximately 1 Hz. For each measurement plane, the time difference between image pairs, δt, is selected such that the maximum particle displacement in the measurement plane is 6 pixels. At each measurement plane, 3000 image pairs are collected in order to ensure statistical convergence for the disk and rotor cases, respectively.

Images are processed using a multi-grid strategy for the stereo cross-correlation with two passes with interrogation area size of 64×64 pixels with 50% overlap followed by three passes with an interrogation area size of 32×32 pixels. Erroneous vectors are removed using a median filter. Spurious vectors are replaced with vectors computed via a Gaussian interpolation of valid neighboring vectors. For all cases, fewer than 2% of vectors are removed and replaced. The uncertainty in the second order statistics was found to be 3% [32].

IV. RESULTS AND DISCUSSION

A. Mean velocity components and mean kinetic energy

Figure 5 shows the mean velocity components and mean kinetic energy surrounding the center turbine in the fourth row of the array. Each subfigure is organized in a similar fashion with the top row of panels in the subfigure representing the rotor case and the bottom row of panels representing the disk case. The rotor hub and disk are located at $x/D = 0$ **with the hub height located at $y/D = 1$**. Figure 5(a) contains the **normalized** streamwise mean velocity component, U/U_{hub}. In both cases, the upstream panels show the persistence of the wake ~~being~~ generated from the third row of the array especially for $x/D \leq -2$. For $x/D \leq -2$, the corresponding downstream region below the top tip ($y/D = 1.5$) has values of U within 5%**,** which is consistent with previous studies indicating that the turbine canopy boundary layer is fully developed by the fourth row in Cartesian turbine arrays [33]. Downstream of the model turbine, a velocity deficit is present in both cases at hub height, $y/D = 1$. While the rotor case shows a larger velocity deficit at hub height and $x/D = 0.6$, it initially recovers at a higher rate so that by $x/D = 1.5$, the ~~percent~~ difference **in U/U_{hub} between the rotor case and disk case** is less than 10%. The similarity of the U-component of the two cases is expected since the matching procedure that was employed is based on this quantity as highlighted in §III.

Figure 5(b) presents the **normalized** vertical mean velocity component, V/V_{hub}. Immediately upstream of both the disk and rotor (e.g. $x/D = 0.3$), positive values of V are present between hub height and top tip as the flow moves upward as a result of the blockage created by the rotor and disk. The V-component is up to 26% different for the rotor and disk **cases** between hub height and the top tip at $x/D = 0.3$. Similarly, negative values of V are present for both cases between hub height and bottom tip as the flow advects downward in response to the blockage of the rotor ~~and~~ **or** disk. Between hub height and top tip at

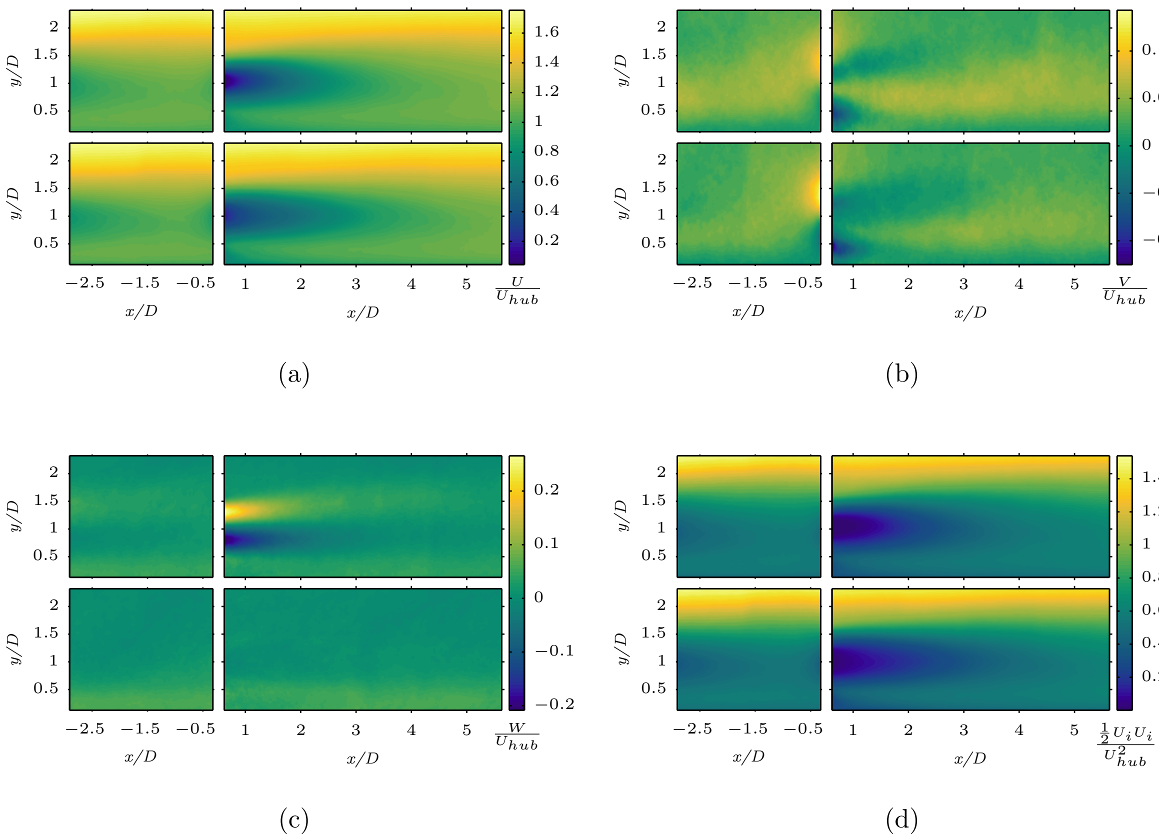

Figure 5. Mean components of velocity and kinetic energy for the center turbine in **the** fourth row. In all subfigures, the inflow and wake of the rotor are in the top row while the bottom row represents the porous disk. (a) normalized streamwise mean velocity (U/U_{hub}), (b) normalized wall normal mean velocity (V/U_{hub}), (c) normalized spanwise mean velocity (W/U_{hub}), (d) normalized mean kinetic energy ($(1/2)U_iU_i/U_{hub}^2$).

streamwise coordinates $x/D < 1.5$, a ~~more extended~~ region ~~having~~ with negative values of V **extends further downstream** ~~is present~~ for the disk case than the rotor case.

The **normalized** spanwise mean velocity component in Figure 5(c) shows the rotation in the rotor case while no such rotational effects due to the disk are present since the disk is stationary. Especially for streamwise coordinates less than $3D$, positive values of W are found above hub height ~~as~~ **where** the rotor blade rotates into the measurement plane and negative values of W below hub height ~~as~~ **where** the blade rotates out of the measurement plane, thus conserving angular momentum. At $x/D = 0.6$, the differences in W between the disk and rotor cases are as large as 190% in the region between the top and bottom tip.

The mean kinetic energy, K, shown in Figure 5(d) has contour lines of similar shape to those displayed for the U-component. Comparing the magnitudes of U, V, and W in Figure 5, it is evident that the maximum value of U is about an order of magnitude greater than either V or W. The larger magnitude of U relative the other mean velocity components results in the U-component dominating the behavior of K with K defined as $K = 1/2(U^2 + V^2 + W^2)$. As a consequence, the trends described above for U are mirrored in K for both the rotor and disk cases.

B. Reynolds stresses and turbulence intensity

Figure 6 displays components of the time-averaged Reynolds stress tensor **and the turbulence intensity, a quantity derived from the normal Reynolds stresses**. The subfigures are organized identically to those described in §IV A with the rotor case in the top panels of each subfigure and the disk case in the bottom panels of each subfigure. For all components of the Reynolds stress tensor, the rotor case has a larger magnitude than the corresponding Reynolds stress component for the disk case for wall normal distances between the top and bottom tip. ~~This indicates that fluctuations represent larger deviations from the mean flow in all directions are present in this region for the rotor than the disk.~~ **This indicates that greater fluctuations from the mean flow are present in the rotor case than for the disk case.** Below $y/D = 0.3$, the ~~percent~~ differences between the disk and rotor are $\leq 15\%$ for all components of the Reynolds stresses with the exception of $\overline{v'w'}$, which suggests that wall effects dominate the flow behavior at these heights.

The streamwise normal component of the Reynolds stress, $\overline{u'u'}$, is illustrated in Figure 6(a). While the overall shapes of the contours for $\overline{u'u'}$ are comparable, they differ in magnitude between the rotor and disk scenarios. In the near wake for both the rotor and disk cases, $\overline{u'u'}$ has a minimum at approximately hub height, $y/D \approx 1$. However, for the disk, this region with low values of $\overline{u'u'}$ is more elongated in the streamwise direction. Near the top tip, $y/D = 1.5$, the maxima in $\overline{u'u'}$ occurs in both the rotor and disk. This larger maximum value for the rotor occurs at $x/D = 1.6$ and is 22% ~~different from~~ **greater than** the disk case at the same coordinates.

Figure 6(b) shows the in-plane Reynolds shear stress, $\overline{u'v'}$, which physically represents the vertical flux of momentum. ~~The in-plane Reynolds shear stress, $\overline{u'v'}$, is shown in Figure 6(b) which physically represents how the vertical flux of momentum~~

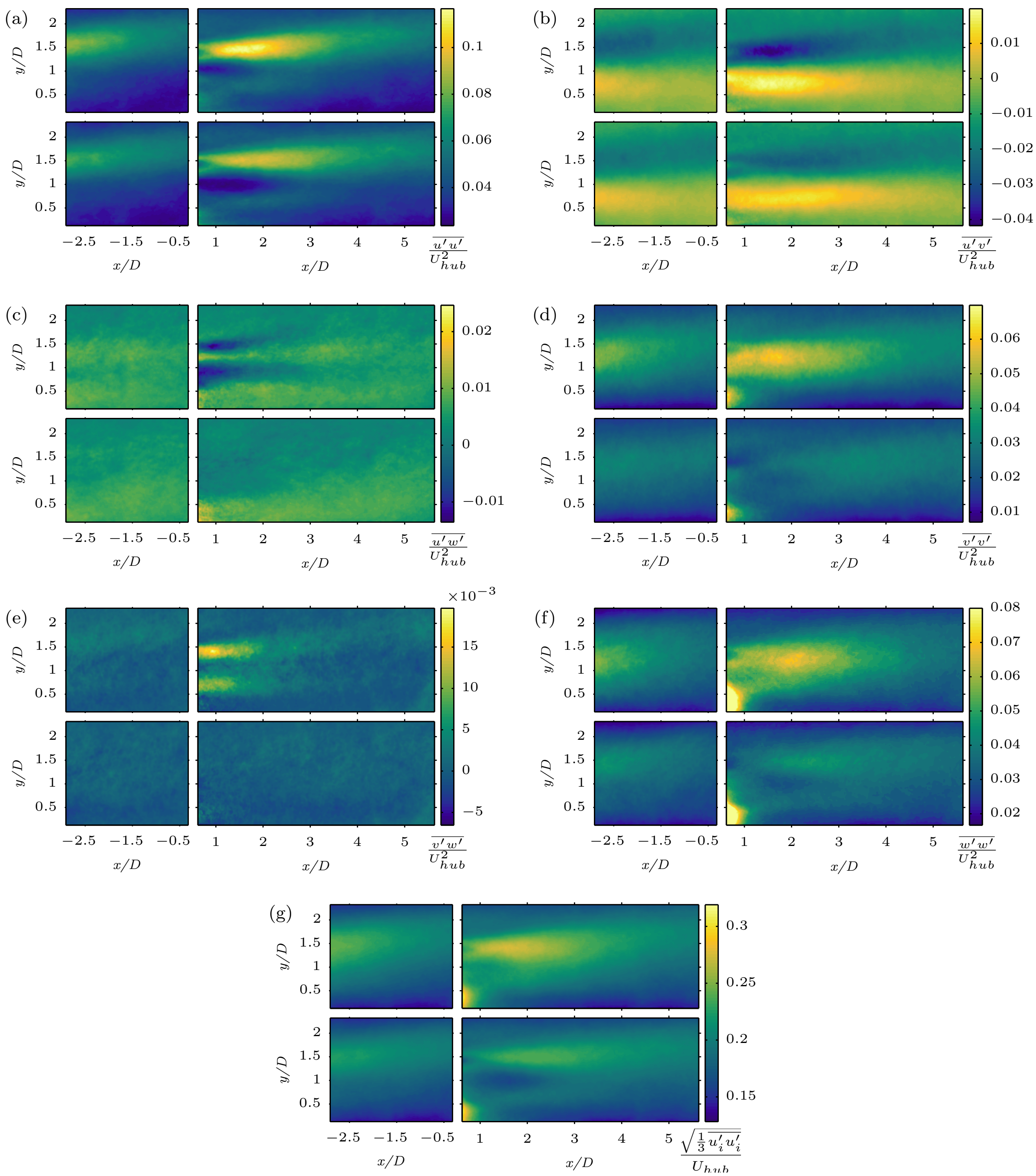

Figure 6. The normalized time-averaged Reynolds stress tensor components $\overline{u_i'u_j'}/U_{hub}^2$ and turbulence intensity $\sqrt{(1/3)\overline{u_i'u_i'}}/U_{hub}$ where i, j = 1, 2, or 3. In each subfigure, the rotor case is represented in the top row while the disk case is represented in the bottom row. (a) $\overline{u'u'}/U_{hub}^2$, (b) $\overline{u'v'}/U_{hub}^2$, (c) $\overline{u'w'}/U_{hub}^2$, (d) $\overline{v'v'}/U_{hub}^2$, (e) $\overline{v'w'}/U_{hub}^2$, (f) $\overline{w'w'}/U_{hub}^2$, (g) $\sqrt{(1/3)\overline{u_i'u_i'}}/U_{hub}$

~~compares for the two schemes.~~ Negative values of $\overline{u'v'}$ indicate a downward flux of momentum whereas positive values ~~are characteristic of~~ **indicate** upward flux of momentum. For both the rotor and disk, $\overline{u'v'}$ changes sign at approximately hub height throughout the measured region downstream of the fourth row. This sign change is present upstream of the fourth row in the segment of the wake that persists from the third row. From approximately bottom tip to hub height, the values of $\overline{u'v'}$ are positive which demonstrates upward momentum flux in this region. On the other hand, from the hub to $y/D = 2.3$, the top-most measurement point, the momentum flux is downward from the higher momentum fluid above the canopy of the array. The magnitudes of $\overline{u'v'}$ differ between the rotor and disk case in the near wake particularly for $x/D \leq 2.8$ where the maxima and minima are more extreme for the rotor. The minimum value of the in-plane shear stress for the rotor of occurs just below top tip at $y/D = 1.45$ at a streamwise coordinate of $x/D = 1.54$ and is 51% different than the value for the disk case at the same spatial coordinates. The maximum of $\overline{u'v'}$ for the rotor wake occurs a $y/D = 0.75$ and a streamwise coordinate of $x/D = 1.6$ and is 40% ~~different from~~ **greater than the** value for the disk case at the corresponding location.

Figure 6(c) presents $\overline{u'w'}$ which demonstrates, for $x/D \lesssim 2$, a pattern of alternating of signs between the bottom and top tip only for the rotor case. This pattern and its implications are further investigated through octant analysis in §IV F. For these streamwise coordinates, just below top tip, the sign of $\overline{u'w'}$ is negative signifying that u' and w' have opposite signs. The shear stress $\overline{u'w'}$ is positive over a narrow feature, which for $x/D = 0.6$ occurs between $1.4 \leq y/D \leq 1.1$, indicating that u' and v' have the same sign in this band. A more extended region having negative values of $\overline{u'w'}$ is then present from hub height to the bottom tip. Within the two regions in which this shear stress is negative, the observed values of $\overline{u'w'}$ for the rotor and disk case differ by as much as 200%.

Like $\overline{u'w'}$, the component $\overline{v'w'}$, shown in Figure 6(e), has an evident pattern in the rotor case only. However, ~~the motif~~ in the near wake**,** ~~in~~ $\overline{v'w'}$ does not ~~consist~~ **have regions** of alternating signs of the stress as in $\overline{u'w'}$. Instead, $\overline{v'w'}$ has two areas of higher magnitude and positive sign just below top tip and just above bottom tip. Positive values of this shear stress signify that v' and w' have the same sign. For the same streamwise coordinate, the Reynolds shear stress component $\overline{v'w'}$ is 1.5-2 times greater in the band at top tip in comparison to the band near bottom tip. Between these two areas, approaching nacelle height, this stress decreases by one to two orders of magnitude.

Figure 6(d) and 6(f) display the wall normal Reynolds stress, $\overline{v'v'}$, and the spanwise

Reynolds stress, $\overline{w'w'}$, respectively. Both normal stresses show the effect of the turbine tower particularly where $x/D \leq 1$ and $y/D \leq 0.7$. The rotor case exhibits higher values for both stresses than the disk case especially heights between bottom and top tip and streamwise coordinates $x/D \leq 3.5$. The maximum ~~percent~~ difference between the rotor and disk is 97% for $\overline{v'v'}$, which occurs at $x/D = 0.62$ and $y/D = 1.42$. For $\overline{w'w'}$, the largest ~~percent~~ difference between the rotor and disk is 70% which is present at $x/D = 1.87$ and $y/D = 1.02$.

The turbulence intensity, *Tu*, based on U_{hub} is shown in Figure 6(g). The turbulence intensity of the disk and rotor cases are qualitatively similar in that both exhibit a region of elevated *Tu* immediately downstream of the tower particularly $y/D \leq 0.4$ and a second region of elevated *Tu* in the vicinity of the top tip ($y/D = 1.5$). In the area immediately downstream of the tower and at wall normal locations $y/D \leq 0.4$, the difference between the rotor and disk cases are below 1%. However, in the vicinity of the top tip, the rotor case exhibits higher turbulence intensities than the disk case which reach a maximum of 26% at $x/D = 0.6$ then decreases and remains in the range of 15-19% for $1 \leq x/D \leq 2$ followed by a monotonic decrease to 7% by $x/D = 3$ and 4% by $x/D = 4$. The largest differences in *Tu* are found bracketing hub height particularly for $1.2 \lesssim x/D \lesssim 2.3$ where the disk case exhibits lower turbulence intensities than the rotor case. The maximum difference in this region is 33% at coordinate $(x/D, y/D) = (1.8, 1.1)$. Since the turbulence intensity based on U_{hub} is represented as $Tu = \sqrt{(1/3)(\overline{u'u'} + \overline{v'v'} + \overline{w'w'})}/U_{hub}$, the features of the turbulence intensity fields of the rotor and disk are derived from their respective Reynolds normal stresses. For example, the area of elevated turbulence intensity immediately downstream of the tower for $y/D \leq 0.4$ is mirrored in $\overline{w'w'}$ and to a lesser degree in $\overline{v'v'}$ for both the rotor and disk cases.

C. Vertical mean kinetic energy flux and production of TKE

Figure 7(a) illustrates the largest term related to the vertical flux of mean kinetic energy, $\overline{u'v'}U$, for the rotor and disk. This figure **is organized in a way that is identical to figures** ~~has the identical organization to those~~ found in §IV A and §IV B with the rotor in the top panels and the disk in the bottom panels. Other components of $\overline{u_i'u_j'}U_i$, where $i = 1$, 2, or 3 and $j = 2$, are smaller by an order of magnitude or more. Given the similarity in U for the disk versus the rotor described in §IV A, the differences **in** ~~between~~ $\overline{u'v'}U$ between the two cases arise from $\overline{u'v'}$, as described in §IV B. Thus, the same trends described in $\overline{u'v'}$ in Figure 6(b) are also present in $\overline{u'v'}U$ in Figure 7(a)~~(b)~~. Cal *et al.* [21] estimated the net vertical flux of kinetic energy into a control volume bounded by the top and bottom rotor tips and found that the result was of the same order of magnitude as the power extracted by the turbine. Notably, in this method, the net kinetic energy flux is proportional to the difference in $\overline{u'v'}U$ between the top and bottom rotor tips. In the present experiment, the difference in streamwise spatial averages is $\langle -\overline{u'v'}U\rangle_x|_{y/D=1.5} - \langle -\overline{u'v'}U\rangle_x|_{y/D=0.5}$ which is 0.91 m^3 s^{-3} for the rotor case and 0.79 m^3 s^{-3} for the disk case representing a ~~percent~~ difference of 13%. The net vertical mean kinetic energy flux for the disk and rotor would be expected to follow this same trend, suggesting a greater net vertical flux for the rotor than the disk.

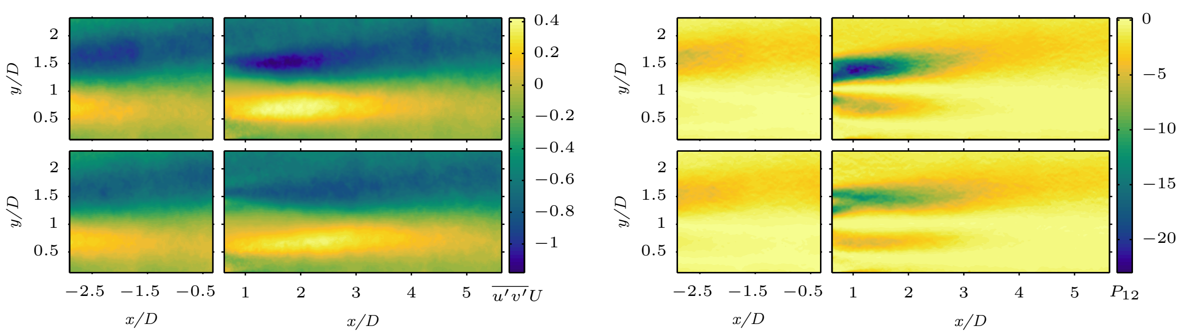

(a) (b)

Figure 7. Largest magnitude components (a) relating to the vertical flux of mean kinetic energy, $\overline{u'v'}U$, and (b) of the production of turbulent kinetic energy tensor, $P_{12} = \overline{u'v'}(\partial U/\partial y)$. The inflow and wake of the rotor **are** in the top row of each subfigure while the bottom panels represent the porous disk. Units are m^3s^{-3} and m^2s^{-3} for $\overline{u'v'}U$ and P_{12}, respectively.

The most significant component of the production of TKE term, $\overline{u'v'}(\partial U/\partial y)$, is represented in Figure 7(b). Considering only measurement locations downstream of the fourth row, the global average of $\overline{u'v'}(\partial U/\partial y)$ is three times greater than the next component closest is magnitude and an order of magnitude greater than the remaining components. For both the rotor and the disk, regions of high magnitude production occur at top tip with a less intense feature just above bottom tip. Elsewhere, production is close to zero. The sign of $\overline{u'v'}(\partial U/\partial y)$ is negative in both of these bands indicating that kinetic energy is being extracted from the mean flow. Especially for $x/D < 2.5$, the rotor case exhibits higher absolute values of production with the maximum at **the** top tip at a streamwise coordinate of $x/D = 1.1$. Here, the greater absolute value of $\overline{u'v'}(\partial U/\partial y)$ for the rotor is 87% different from the corresponding absolute value for disk. These high production areas likely arise from vortex breakdown. Interaction of vortices shed at **the** bottom tip with the tower would be expected to cause production of TKE to be of a smaller magnitude near bottom tip.

D. Determining the region in the wake where rotation is of most importance

The most evident difference between the rotor and disk case~~s~~ is due to the rotation of the rotor**,** which is shown in the mean spanwise velocity component, W, in Figure 5(c). Thus, the mean kinetic energy budget is analyzed by separating the downstream measurements into two segments based on W. The criteria for determining the location at which to divide the downstream measurements was made by evaluating the vertical average of the absolute value of W represented as $\langle|W|\rangle_y$ between the top tip ($y/D = 1.5$) and bottom tip ($y/D = 0.5$). Thereafter, the derivative of $\langle|W|\rangle_y$ with respect to the streamwise coordinate was obtained using a second order central differencing scheme to yield $d\langle|W|\rangle_y/dx$. After a steep change in magnitude in the region $0.6 \leq x/D \lesssim 3$, $d\langle|W|\rangle_y/dx$ ~~reached a value which~~ oscillates~~d~~ about zero by streamwise coordinate $x/D \approx 3$. This indicates that **only small changes in** W ~~changes slowly in a linear fashion~~ **occur** for $x/D \gtrsim 3$. These trends are evident in Figure 4(c). Due to the amplification of noise in W from to the computation of the derivative, a polynomial line of best fit of $d\langle|W|\rangle_y/dx$ was utilized to aid in a precise determination of the streamwise coordinate at which $d\langle|W|\rangle_y/dx$ reaches a near constant value. Based on the line of best fit, this streamwise coordinate is $x/D = 3.2$. Given these changes in $\langle|W|\rangle_y$ as a function of streamwise coordinate, the region $0.6 \leq x/D \leq 3.2$ represents the region of the wake where rotation is most important while the region $3.2 < x/D \leq 5.6$ delineates the region where rotation is less important.

E. Mean kinetic energy budget as a function of rotational effects

The terms in the mean kinetic energy budget are computed and horizontally averaged in the two regions $0.6 \leq x/D \leq 3.2$ and $3.2 < x/D \leq 5.6$ to create the vertical profiles shown in Figure 8. Components requiring partial derivatives with respect to z are not included nor is the **term representing** transport due to the local pressure gradient ~~represented~~ **depicted**. The dissipation term, $2\nu S_{ij}S_{ij}$, and the term representing transport due to viscosity, $2\nu\partial S_{ij}U_i/\partial x_j$, are of the order 10^{-3} and 10^{-2} or less, respectively. Thus, both of these quantities appear to be zero on the scale used in Figure 8.

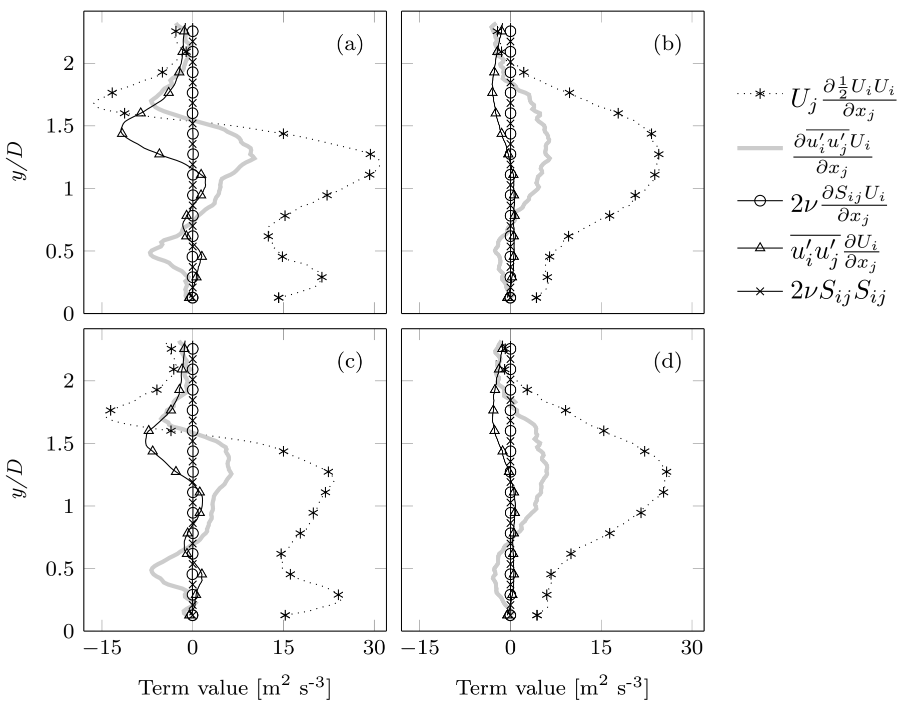

Figure 8. Horizontal averages of terms in the mean kinetic energy budget in the region where rotation is most important, $0.6 \leq x/D \leq 3.2$, for (a) the rotor and (c) disk. The corresponding horizontal averages in the region where rotation is less important, $3.2 < x/D \leq 5.6$, for the (b) rotor and (d) disk.

~~Peak values of the terms represented in Figure 8 are comparable and~~. ~~t~~**T**he wall normal location of the~~se~~ peak~~s~~ **values represented in Figure 8** for the rotor and disk are within $0.06D$ of one another. In the vicinity of the top tip, the peak value of advection, $U_j\partial K/\partial x_j$, for the rotor is -16.4 m^{2}s^{-3} at $y/D = 1.68$ and -14.7 m^{3}s^{-3} at $y/D = 1.73$ for the disk which represents a ~~percent~~ difference of 11%. Recall, $K = 1/2(U_iU_i)$, where $i = 1, 2$, or 3. Also near the top tip, for the **term representing** transport via turbulence ~~term~~, $\partial\overline{u_i'u_j'}U/\partial x_j$, is 28% different between the rotor and disk **with** peak values in $0.6 \leq x/D \leq 3.2$, while the percent difference in the peak values for the disk and rotor are 6% ~~different~~ for $3.2 < x/D \leq 5.6$. Similar trends are observed for peak values near **the** top tip for the production term, $\overline{u_i'u_j'}\partial U_i/\partial x_j$, which **are** ~~has~~ 41% differen**t**~~ce~~ in $0.6 \leq x/D \leq 3.2$ and ~~a percent difference of~~ 2% **different** in $3.2 < x/D \leq 5.6$. For heights between the top and bottom tip, the ~~percent~~ difference in the peak value of the advection term for $0.6 \leq x/D \leq 3.2$ is 28%, which decreases to a ~~percent~~ difference of 7% in $3.2 < x/D \leq 5.6$. Also between the bottom and top tip, the ~~percent~~ difference in the **term representing** transport via turbulence ~~term~~ is 45% ~~different~~ in $3.2 < x/D \leq 5.6$ which declines to a difference of 6% in $3.2 < x/D \leq 5.6$. Thus, while significant percent differences are present in the region where rotation is most important ($0.6 \leq x/D \leq 3.2$), these differences are mitigated in the region where rotation is less important ($3.2 < x/D \leq 5.6$) to the extent that the mean kinetic energy transport terms are nearly equivalent in the region where rotation is less important.

F. Conditional averaging of $\overline{u'v'}U$ via octant analysis

Octant analysis of $\overline{u'v'}U$ yields the conditionally averaged quantity $\ddot{\overline{u'v'U}}$ which is shown in Figure 9. The top row of subfigures in Figure 9, (a) and (b), represent~~s~~ the rotor in the near and far wake, respectively. Similarly, the bottom row of subfigures, (c) and (d), illustrate~~s~~ **the** disk for the near and far wake, respectively. Furthermore, the arrangement of of the eight panels in each subfigure corresponds with the variation in the signs of u', v', and w' shown in Figure 1. This conditional averaging was done as outlined in Eq. (2). The summation of $\ddot{\overline{u'v'U}}$ over all eight octants in Figure 9(a) yields $\overline{u'v'}U$ shown in Figure 6(a) for $0.6 \leq x/D \leq 2$. The same summation can **be** done over all octants for $\ddot{\overline{u'v'U}}$ in the far wake **of the rotor case** shown in Figure 9(b) and for the disk case~~s~~ in Figure 9(c)-(d) to arrive at the corresponding values of $\overline{u'v'}U$.

Octant analysis for the rotor case corroborate**s** and also extend**s** previous work in quadrant analysis of wind turbine wakes [26], [27]. These previous works showed that ejections ($u' < 0$, $v' > 0$) and sweeps ($u' > 0$, $v' < 0$) dominate the vertical mean kinetic energy transport into the swept area of the rotor. ~~Viestenz [27] found that the maxima for ejections that lead to vertical kinetic energy flux are present at and just above the rotor while maxima~~

~~for sweeps are just below top tip.~~ **Viestenz [27] found a maximum for ejections just above the top tip and a maximum for sweeps just below the top tip. Both of these maxima contribute to vertical kinetic energy flux.** In the present work, octant analysis reveals the role that w' plays in ~~these~~ ejections ($O2$ and $O5$) and sweeps ($O4$ and $O8$) **in the vicinity of the top tip**. **For the rotor case,** a~~A~~ maxim**um**~~a~~ in the magnitude of $\overline{u'v'\ddot{U}}$ is present at **the** top tip in Figure 9(a) for ejections ~~but only for ejections in which the sign of w' is positive as in $O2$.~~ **However, it is primarily ejections in $O2$, which have a positive sign for w', that contribute to this maximum for the rotor case.** Ejections in $O2$ represent situations where the direction of ~~the fluctuation~~ w' is in the direction opposite that of the rotor rotation at **the** top tip. ~~For sweeps, a maximum is also found in Figure 9(a) just below top tip, but only for sweeps in $O5$ which possess a negative sign of w'.~~ **Similarly, a maximum is found just below the top tip in Figure 9(a) for sweeps in the rotor case. This maximum is dominated by sweeps in $O5$, which possess a negative sign for w'.**

The observation in the rotor case that ejections at **the** top tip have a preference for $O2$ while sweeps at **the** top tip have a preference for $O8$ is in accordance with patterns found in the Reynolds shear stresses $\overline{u'w'}$ and $\overline{v'w'}$ (see §IV B). Specifically, the presence of top tip ejections in $O2$, where $u' < 0$ and $w' > 0$, and top tip sweeps in $O8$, where $u' > 0$ and $w' < 0$, agrees with the negative sign of $\overline{u'w'}$ observed at **the** top tip in Figure 6(c). This octant preference for top tip ejections and sweeps is also in agreement with the positive sign of $\overline{v'w'}$ at this location for the rotor in Figure 6(e). Although the maximum positive value of $\overline{v'w'}$ is found just below **the** top tip, this region in which $\overline{v'w'}$ is positive extends above the rotor tip.

One physical mechanism that would cause a preference for a specific sign of w' for sweeps and ejections near the top tip is related to the periodic nature of the blockage by the rotor. As the blade passes through its topmost position and is within the PIV plane, blockage by the blade would be expected to tend to reduce the instantaneous local streamwise velocity to a value smaller than the ensemble average (U) leading to a negative value of u'. Since fluctuations are centered about the mean, any instantaneous velocity smaller than the ensemble mean corresponds to a negative value of the fluctuation while an instantaneous velocity greater than the ensemble average generates a positive value of the

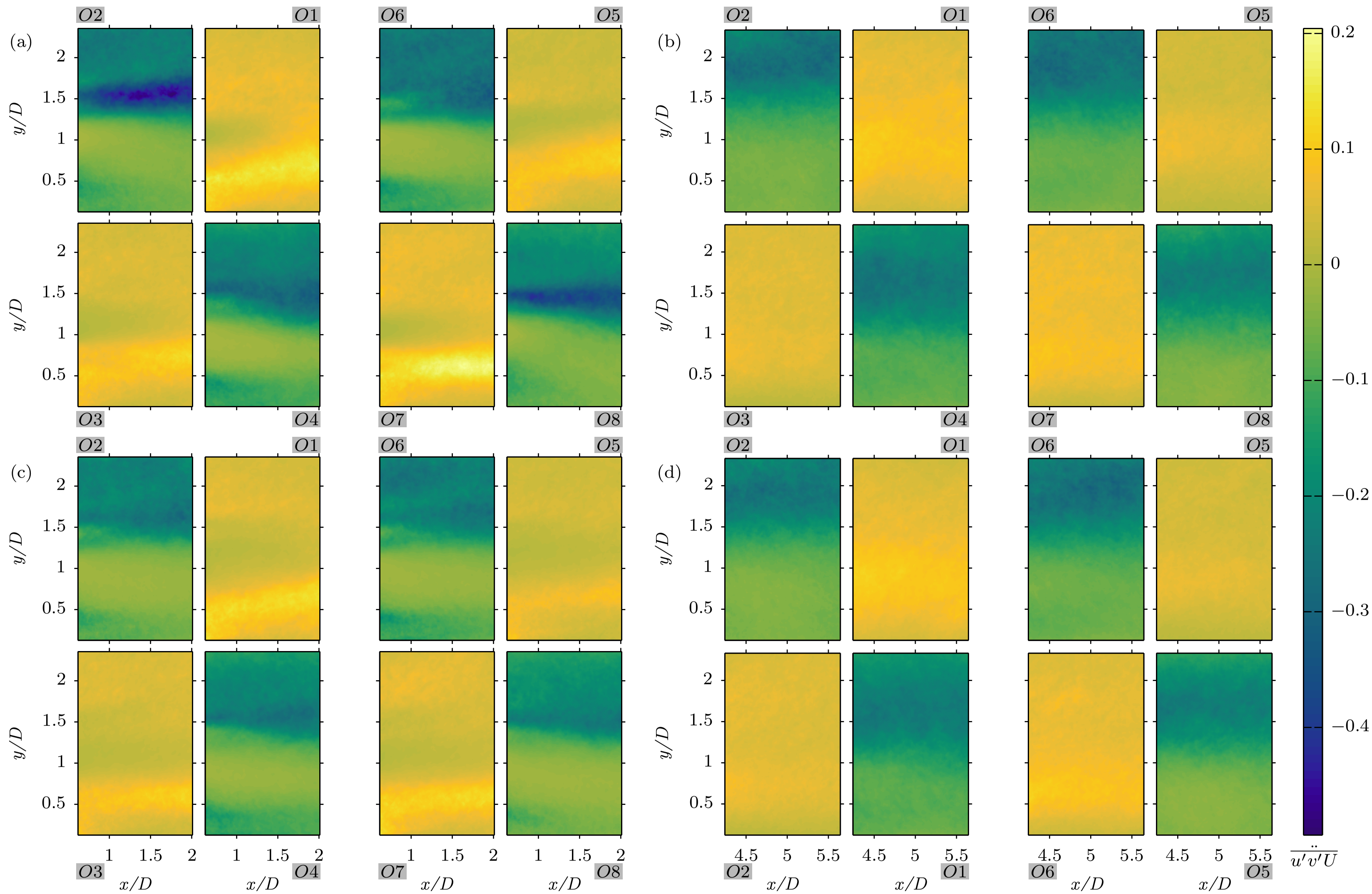

Figure 9. Conditional averages of the vertical mean kinetic energy flux ($\overline{u'v'\ddot{U}}$) for each octant. Rotor results are given for (a) the near wake and (b) the far wake. Results for the disk are provided in (c) the near wake and (d) the far wake. Subfigures (a)-(d) all have a common arrangement of eight panels organized according to the signs of u', v', and w' as in Figure 1. Octants 1-4 have positive signs of w' while octants 4-8 have negative signs of w'.

fluctuation. Furthermore, the position of the blade in the PIV plane would tend to cause the value of the instantaneous vertical velocity near the top tip to be larger than the ensemble average V as the flow is deflected upwards over the blade tip leading to a positive deviation of v'. At this same point in time, the instantaneous spanwise velocity measured in the PIV plane would be expected to be larger than the ensemble average W due to the close proximity of the blade and angular velocity imparted by the blade. Such a tendency for larger instantaneous values of the spanwise velocity would lead to positive values of w'. This combination of signs for the velocity fluctuations produces sweeps in $O2$ and may explain why ejections in $O2$ are more predominant than ejections in $O6$ in the vicinity of $y/D = 1.5$.

In contrast, when the rotor blade has passed its topmost position, the absence of a blockage in the PIV plane would be expected to tend to cause streamwise velocities near the top tip to have instantaneous values that are larger than U leading to positive values of u'. Similarly, the absence of the blade would tend to produce instantaneous vertical velocities that are lower than V since the flow is not deflected by the blade. These instantaneous vertical velocities which are smaller than V correspond to negative values of v'. Concurrently, the absence of the blade at its topmost position would be tend to lead to instantaneous spanwise velocities locally that are smaller than W due to the lack of rotational influence of the blade. Instantaneous spanwise velocities that are smaller than W correspond to negative values of w'. This combination of the signs of the fluctuations leads to sweeps in $O8$ and may provide insight as to why sweeps at the top tip in $O8$ are more dominant than those in $O2$. The relative vertical displacement of the maxima near top tip for ejections and sweeps is also consistent with this physical mechanism.

Two trends are present in Figure 9. One trend is that the disparities between $\overline{u'v'\ddot{U}}$ in the same octant for the rotor versus the disk decrease moving from the near wake to the far wake. For example, compare $\overline{u'v'\ddot{U}}$ in $O2$ for the rotor in the near wake in Figure 9(a) with $O2$ for the disk in the near wake shown in Figure 9(c) especially near the top tip, $y/D = 1.5$. **Secondly,** ~~The second tendency is~~ for the rotor case itself, differences between ~~the~~ octants with the same sign of u' and v' but opposite signs of w' also decrease in moving from the near wake to the far wake. For example, compare $O2$ with $O6$ in the near wake in Figure 9(a) and then compare $O2$ with $O6$ in the far wake in Figure 9(b). Significant variations in $\overline{u'\ddot{v}'U}$ between such corresponding octants in the rotor case in ~~only~~ the near wake indicate **that** a strong preference for a particular sign of w' is associated with vertical mean kinetic energy flux and that this preference is related to the rotation of the rotor. Two features of Figure 9 suggest that the rotationality of the rotor does not heavily impact vertical mean kinetic energy transport in the far wake: 1) the absence of a strong preference for a particular sign of w' illustrated by the comparable values of $\overline{u'\ddot{v}'U}$ found between corresponding octants in the far wake in the rotor case and 2) the ~~congruence~~ **agreement** between the rotor and disk octants in the far wake.

Since $\overline{u'\ddot{v}'U}$ is related to the vertical transport of mean kinetic energy, inferences can be made regarding transport from these results. Specifically, these observations point towards the idea that the instantaneous directionality of the fluctuations that lead to vertical kinetic energy transport are quite different in the region nearest the turbine where rotation is important and are then minimized in the far wake. In addition, these results imply a difference in the flow structure that occurs concurrently with vertical mean kinetic transport in the near wake and a curtailment of these flow structure differences associated with transport in the far wake.

A quantitative comparison of the octant analysis results for **the** rotor and disk **cases** as a function of downstream streamwise distance is shown in Figure 10. From the octant analysis of $\overline{u'v'U}$ for each of the downstream PIV planes, the percent difference at every measurement point between $\boldsymbol{\overline{u'\ddot{v}'U}}$ for the disk and rotor in each octant was calculated. For the region between **the** top and bottom tip, the resulting percent differences of $\boldsymbol{\overline{u'\ddot{v}'U}}$ in ~~a~~ each octant were then averaged to arrive at the average percent differences displayed in Figure 10. This method was applied to each of the four downstream PIV measurement planes. The average percent differences between the same octant for the rotor and disk decrease from a maximum of 68% in $0.6 \leq x/D \leq 1.9$ to a maximum of 17% in the furthest downstream plane ($4.3 \leq x/D \leq 5.6$). The asymmetry of these average percent differences decreases moving downstream**,** which can be seen by comparing octants with the same signs of u' and v' but differing signs of w'. For example, compare the magnitude of the averages in $O3$ versus $O7$ at streamwise coordinates $0.6 \leq x/D \leq 1.9$ to those in $O3$ versus $O7$ at streamwise coordinates $4.3 \leq x/D \leq 5.6$. This reduction in asymmetry moving downstream indicates decreased preference for a particular sign of w'.

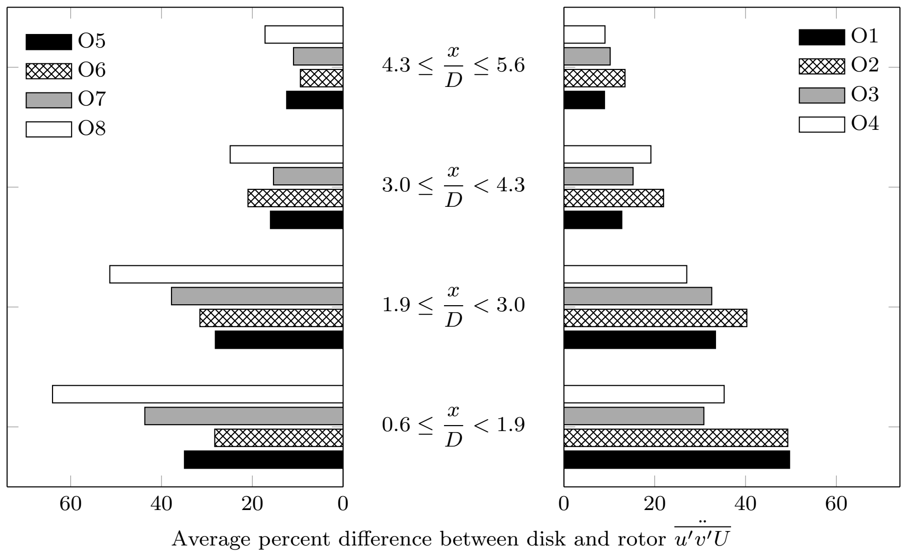

Figure 10. Average percent difference between $\overline{u'v'\ddot{U}}$ for the disk and rotor in each octant as a function of downstream streamwise distance. Only data between the top ($y/D = 1.5$) and bottom tip ($y/D = 0.5$) is considered. As downstream distance increases, differences decrease and average percent difference become more symmetric with respect to **the** sign of w'.

V. CONCLUSIONS

Within a model wind farm, the wake of a model turbine with a three-bladed rotor is compared to the wake produced by a matched porous disk. ~~The wake of a model turbine with a rotor and a porous disk when these models are placed in array are compared.~~ **The** ~~M~~**m**ean velocity components, Reynolds stresses, mean kinetic energy **budget**~~transport~~, and an octant analysis of the term most relevant to vertical transport of mean kinetic energy are used to make a detailed comparison of the flow physics in the two cases. The main difference in the mean velocity components is found to be the W-component, which results from rotation of the rotor. The Reynolds normal stresses share the same features for the rotor and disk although normal stresses have consistently higher magnitudes for the rotor between **the** top and bottom tip especially for $x/D \leq 3.5$. The same comments apply for the shear stress $\overline{u'v'}$. **The variation in the normal stresses leads to a higher turbulence intensity in this area for the rotor than the disk.**

In contrast, shear stresses involving w' have altogether different patterns of features for the disk and rotor in the near wake.

Discrepancies between the rotor and disk cases in terms of the normal stresses and thus the turbulence intensity are noteworthy because of the potential impact on the inflow of downwind turbines. The dynamic loads and fatigue characteristics of wind turbines are impacted by the turbulence intensity of the inflow [5]. Furthermore, modification of the turbine structural support to account for turbulence intensity increases caused by upstream wakes had been found to be advantageous under some circumstances in offshore farms [34]. Turbine control schemes are also related to the inflow of turbines throughout the wind farm [35], [36]. The present results suggest that the reduced normal stresses and turbulence intensity observed in the disk case are primarily a concern for scenarios in which a stationary disk parameterization for the rotor is used in computational simulations of farms where the spacing is less than $3-4D$. However, this specific spacing would be influenced by atmospheric conditions since atmospheric conditions have been found to impact wake recovery and modulate the inflow to downstream turbines [37]. Although some operational wind farms such as Middelgrunden have a turbine spacing that is within this $3-4D$ range [38], the present results suggest that farms with a larger turbine-to-turbine spacing would be adequately represented using rotor parameterizations which involve a stationary disk.

Examining the W-component for the rotor case, rotational effects are evident particularly in the region $0.6 \leq x/D \leq 3.2$ and are absent in the disk case. In this same region where rotation has the greatest influence, differences in the peak values of mean kinetic energy transport terms are as large as 41% percent different to as small as 3% different. In contrast, in the region where rotation was found to be less important, percent differences in the peak values of the mean kinetic energy transport terms were found to range from a percent difference of 6% at most to 2% at the least. In the segment of the wake where rotation is most important, the greatest disparities are found in the production of TKE term in the vicinity of the top tip. In comparison to the disk, the rotor case has a greater production of TKE indicating more kinetic energy is extracted from the mean flow in the swept area of the rotor. However, this efflux of mean kinetic energy in the rotor case is offset by a greater transport of kinetic energy by turbulence. Thus, in the region of the wake where rotation is less important, the terms in the mean kinetic energy equation are nearly equivalent while significant discrepancies exist were rotation is a crucial characteristic.

Conditional averaging of $\overline{u'v'U}$ to obtain $\ddot{\overline{u'v'U}}$ using an octant analysis approach is done in order to examine the directionality of the velocity fluctuations from the mean that are associated with the vertical flux of mean kinetic energy. At measurement locations nearest the turbine model, evident preferences for certain signs of w' are present in the rotor case and are minimized in the disk case. Such a preference is particularly apparent at the rotor top tip where the maximum magnitude of $\ddot{\overline{u'v'U}}$ is found in octant 2 where $w' > 0$. In contrast, just below top tip for the rotor, the maximum magnitude of $\ddot{\overline{u'v'U}}$ is found in octant 8 where $w' < 0$. Disparities in $\ddot{\overline{u'v'U}}$ between the rotor and disk in the same octant is an indication that the flow structures associated with vertical mean kinetic energy flux are different in the near wake for the rotor than for the disk. However, such differences are not as evident in the far wake.

The mean kinetic energy budget and octant analysis suggest that rotor and disk cases interact with the atmosphere aloft distinctly differently in the region of the wake where rotation is a key flow feature. The mean kinetic energy budget indicates that the vertical entrainment of mean kinetic energy from the fluid above the farm at the top tip is lower in the disk case than in the rotor case. Octant analysis indicates that mechanism responsible for this entrainment is dissimilar for the rotor and disk cases. However, determining the details of this mechanism requires elucidation of the flow structure responsible. Together, these two analyses imply that studies which seek to examine the details of the interaction of farms with the atmosphere would benefit from an rotor parameterization which represents rotational effects.

The comparable nature of the results **using the present two mean kinetic energy analysis techniques points** to the idea that the that the flow is nearly the same from the perspective of the mean velocity and mean kinetic energy equation in regions where rotation is not a critical phenomenon. To extend these results to modeling applications, it is important to consider that the inflow conditions and simulated atmospheric conditions would be expected to heavily impact the extent of the wake that is highly influenced by rotation. For example, in highly turbulent and convective atmospheric conditions, this region would be expected to be shorter than in conditions that were more quiescent. Thus, a criteria akin to the one applied in the present work would be advantageous in order to apply the present conclusions in other scenarios. Overall, these results are encouraging for modelers who employ the actuator disk model for simulations of wind farms and are therefore addressing questions that are related to the mean energetics of the flow.

ACKNOWLEDGMENTS

Vasant Vuppuluri is acknowledged for his help in disk characterization and experimental set up. This work was funded by the National Science Foundation (NSF-CBET-1034581).

---

[1] Global Wind Energy Council. Global Wind Report Annual Market Update 2014. Technical report, February 2015.

[2] L. P. Chamorro and F. Porté-Agel. A wind-tunnel investigation of wind-turbine wakes: boundary-layer turbulence effects. *Boundary-layer meteorology*, 132(1):129–149, 2009.

[3] R. J. Barthelmie, S. C. Pryor, S. T. Frandsen, K. S. Hansen, J. G. Schepers, K. Rados, W. Schlez, A. Neubert, L. E. Jensen, and S. Neckelmann. Quantifying the Impact of Wind Turbine Wakes on Power Output at Offshore Wind Farms. *Journal of Atmospheric and Oceanic Technology*, 27(8):1302–1317, 2010.

[4] N. Hamilton, M. Melius, and R. B. Cal. Wind turbine boundary layer arrays for Cartesian and staggered configurations-Part I, flow field and power measurements. *Wind Energy*, 18(2):277–295, 2015.

[5] W. Tian, A. Ozbay, and H. Hu. Effects of incoming surface wind conditions on the wake characteristics and dynamic wind loads acting on a wind turbine model. *Physics of Fluids*, 26(12):125108, 2014.

[6] S. Lee, M. Churchfield, P. Moriarty, J. Jonkman, and J. Michalakes. Atmospheric and Wake Turbulence Impacts on Wind Turbine Fatigue Loadings. Nashville, Tennessee, January 2012. American Institute of Aeronautics and Astronautics.

[7] W. Zhang, C. D. Markfort, and F. Porté-Agel. Experimental study of the impact of large-scale wind farms on landatmosphere exchanges. *Environmental Research Letters*, 8(1):015002, 2013.

[8] S. B. Roy and J. J. Traiteur. Impacts of wind farms on surface air temperatures. *Proceedings of the National Academy of Sciences*, 107(42):17899–17904, 2010.

[9] L. J. Vermeer, J. N. Sørensen, and A. Crespo. Wind turbine wake aerodynamics. *Progress in Aerospace Sciences*, 39(6-7):467–510, 2003.

[10] B. Sanderse, S. P. van der Pijl, and B. Koren. Review of computational fluid dynamics for wind turbine wake aerodynamics. *Wind Energy*, 14(7):799–819, 2011.

[11] J. N. Sørensen. Aerodynamic Aspects of Wind Energy Conversion. *Annual Review of Fluid Mechanics*, 43(1):427–448, 2011.

[12] Y.-T. Wu and F. Porté-Agel. Large-Eddy Simulation of Wind-Turbine Wakes: Evaluation of Turbine Parametrisations. *Boundary-Layer Meteorology*, 138(3):345–366, 2011.

[13] L. A. Martínez-Tossas, M. J. Churchfield, and S. Leonardi. Large eddy simulations of the flow past wind turbines: actuator line and disk modeling. *Wind Energy*, 18(6):1047–1060, 2015.

[14] P.-Å. Krogstad and P. E. Eriksen. Blind test calculations of the performance and wake development for a model wind turbine. *Renewable Energy*, 50:325–333, 2013.

[15] F. N. Coton, T. Wang, and R. A. McD. Galbraith. An examination of key aerodynamic modelling issues raised by the NREL blind comparison. *Wind Energy*, 5(2-3):199–212, 2002.

[16] S. Schreck. The NREL full-scale wind tunnel experiment: Introduction to the special issue. *Wind Energy*, 5(2-3):77–84, 2002.

[17] S. Aubrun, P. Devinant, and G. Espana. Physical modelling of the far wake from wind turbines. Application to wind turbine interactions. In *Proceedings of the European Wind Energy Conference, Milan, Italy*, pages 7–10, 2007.

[18] L. E. M. Lignarolo, D. Ragni, C. J. Simão Ferreira, and G. J. W. van Bussel. Kinetic energy entrainment in wind turbine and actuator disc wakes: an experimental analysis. *Journal of Physics: Conference Series*, 524(1):012163, June 2014.

[19] R. J. Barthelmie and L. E. Jensen. Evaluation of wind farm efficiency and wind turbine wakes at the Nysted offshore wind farm. *Wind Energy*, 13(6):573–586, 2010.

[20] M. Calaf, C. Meneveau, and J. Meyers. Large eddy simulation study of fully developed wind-turbine array boundary layers. *Physics of Fluids*, 22(1):015110, 2010.

[21] R. B. Cal, J. Lebrón, L. Castillo, H. S. Kang, and C. Meneveau. Experimental study of the horizontally averaged flow structure in a model wind-turbine array boundary layer. *Journal of Renewable & Sustainable Energy*, 2(1):013106, 2010.

[22] M. Abkar and F. Porté-Agel. Mean and turbulent kinetic energy budgets inside and above very large wind farms under conventionally-neutral condition. *Renewable Energy*, 70:142–152, 2014.

[23] J. M. Wallace, H. Eckelmann, and R. S. Brodkey. The wall region in turbulent shear flow. *Journal of Fluid Mechanics*, 54(1):39–48, 1972.

[24] S. M. Ölçmen, R. L. Simpson, and J. W. Newby. Octant analysis based structural relations for three-dimensional turbulent boundary layers. *Physics of Fluids*, 18(2):025106, 2006.

[25] M. M. Madden Jr. *Octant analysis of the Reynolds stresses in the three dimensional turbulent boundary layer of a prolate spheroid*. PhD thesis, Virginia Polytechnic Institute, Blacksburg, Virginia, 1997.

[26] N. Hamilton, H. S. Kang, C. Meneveau, and R. B. Cal. Statistical analysis of kinetic energy entrainment in a model wind turbine array boundary layer. *Journal of Renewable & Sustainable Energy*, 4(6):063105, 2012.

[27] K. Viestenz and R. B. Cal. Streamwise Evolution of statistical events in a model wind-turbine array. *Boundary-Layer Meteorology*, 158(2):1–19, 2015.

[28] L. E. M. Lignarolo, D. Ragni, F. Scarano, C. J. Simão Ferreira, and G. J. W. van Bussel. Tip-vortex instability and turbulent mixing in wind-turbine wakes. *Journal of Fluid Mechanics*, 781:467–493, 2015.

[29] N. Hamilton and R. B. Cal. Anisotropy of the Reynolds stress tensor in the wakes of wind turbine arrays in Cartesian arrangements with counter-rotating rotors. *Physics of Fluids*, 27(1):015102, 2015.

[30] T. Burton, N. Jenkins, D. Sharpe, and E. Bossanyi. *Wind Energy Handbook*. Wiley, 2 edition, 2011.

[31] B. Wieneke. Stereo-PIV using self-calibration on particle images. *Experiments in Fluids*, 39(2):267–280, 2005.

[32] W. K. George Jr., P. D. Beuther, and J. L. Lumley. Processing of random signals. In *Proceedings of the Dynamic Flow Conference 1978 on Dynamic Measurements in Unsteady Flows*, pages 757–800. Springer, 1978.

[33] L. P. Chamorro and F. Porté-Agel. Turbulent flow inside and above a wind farm: a wind-tunnel study. *Energies*, 4(11):1916–1936, 2011.

[34] R. A. G. Tejada. *Effects on support structure design due to wake-generated turbulence*. MS

thesis, Delft University of Technology, Delft, The Netherlands, 2014.

[35] J. Annoni, P. Seiler, K. Johnson, P. Fleming, and P. Gebraad. Evaluating wake models for wind farm control. In *American Control Conference (ACC), 2014*, pages 2517–2523. IEEE, 2014.

[36] P. Fleming, A. Ning, P. Gebraad, and K. Dykes. Wind plant system engineering through optimization of layout and yaw control. *Wind Energy*, 19(2):329–344, 2016.

[37] M. J. Churchfield, S. Lee, J. Michalakes, and P. J. Moriarty. A numerical study of the effects of atmospheric and wake turbulence on wind turbine dynamics. *Journal of Turbulence*, 13(14):1–32, 2012.

[38] R. J. Barthelmie, S. T. Frandsen, M. N. Nielsen, S. C. Pryor, P.-E. Rethore, and H. E. Jrgensen. Modelling and measurements of power losses and turbulence intensity in wind turbine wakes at Middelgrunden offshore wind farm. *Wind Energy*, 10(6):517–528, 2007.